

Article

Electrolyte engineering for highly inorganic solid electrolyte interphase in high-performance lithium metal batteries

Yan Zhao, Tianhong Zhou, Lars P.H. Jeurgens, Xian Kong, Jang Wook Choi, Ali Coskun

jangwookchoi@snu.ac.kr (J.W.C.)
ali.coskun@unifr.ch (A.C.)

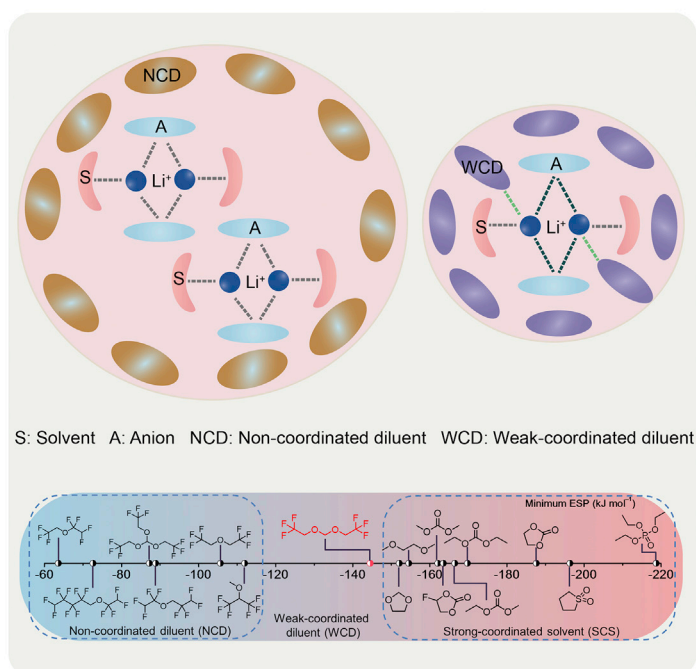
Highlights

Introducing the concept of weakly coordinated diluents for electrolyte engineering

Accelerating anion decomposition by weakly coordinated diluents

Ultra-high Li_2O formation in the solid electrolyte interphase to realize high CE

Revealed the critical role of small solvent-salt cluster formation in the electrolyte



We introduced the concept of weak-coordinated diluent (WCD), which represents the electrostatic potential region between non-coordinated diluents (NCD) and strong-coordinated solvents. Localized high-concentration electrolytes incorporating WCD formed smaller solvent-salt clusters and exhibited accelerated anion decomposition kinetics promoted by the weakened FSI anion- Li^+ coordination and lower affinity of WCD toward the anion to realize homogeneously distributed, ultra-high Li_2O content in solid electrolyte interphase, to achieve a high average Coulombic efficiency of 99.72%, and to achieve a very good cycling performance in the $\text{Li}|\text{LiNi}_{0.8}\text{Co}_{0.1}\text{Mn}_{0.1}\text{O}_2$ full cell.



Article

Electrolyte engineering for highly inorganic solid electrolyte interphase in high-performance lithium metal batteries

Yan Zhao,^{1,5} Tianhong Zhou,^{1,5} Lars P.H. Jeurgens,² Xian Kong,³ Jang Wook Choi,^{4,*} and Ali Coskun^{1,6,*}

SUMMARY

Electrolytes play pivotal roles in the stabilization of Li metal surface and operation at high voltages. In particular, localized high-concentration electrolytes have outperformed state-of-the-art electrolytes due to their unique solvation structures. However, a direct correlation between solvation structure in LHCEs, in particular for weakly coordinated diluents, and SEI composition is not well understood, yet it is highly critical to realize high Coulombic efficiency (CE) beyond 99.5%. Here, a class of electrolyte based on bis(2,2,2-trifluoroethoxy)methane and 1,2-dimethoxyethane was introduced to regulate anion decomposition to achieve ultra-high Li₂O content of 63% in the SEI along with a highly uniform phase distribution. These unique features enabled a record-high CE of 99.72% and proved the impact of homogeneously distributed high Li₂O SEI. The related Li|LiNi_{0.8}Co_{0.1}Mn_{0.1}O₂ full cell with a negative/positive capacity ratio of 2.5 achieved 90% capacity retention after 200 cycles at 1 C and 80% retention after 596 cycles at 3 C.

INTRODUCTION

The successful commercialization of lithium-ion batteries (LIBs) has had a profound impact on our daily lives by advancing a wide range of applications from portable electronics to electrical vehicles to smart grids. Although the demand for high-energy-density LIBs has increased significantly in recent years, conventional LIBs based on a graphite anode (372 mAh g⁻¹)^{1–4} cannot keep up with this demand as they appear to have reached their limits in terms of energy storage capacity. In this sense, Li metal is the ultimate anode choice due to its low density (0.59 g cm⁻³), low electrode potential (–3.04 V vs. the standard hydrogen electrode), and extremely high specific capacity (3,860 mAh g⁻¹), which could double the energy density (~500 Wh kg⁻¹) over current LIBs when paired with high-voltage cathode materials such as LiNi_xCo_yMn_{1–x–y}O₂ (Ni-rich NCM, Ni ≥ 60%).^{3,5–7} However, the thermodynamic instability of organic solvents, represented by carbonates, toward lithium metal anode (LMA) causes continuous side reactions, such as consuming Li metal and electrolyte, thus leading to the formation of a non-uniform, mechanically weak solid electrolyte interphase (SEI) layer, Li dendrites, and consequent short cycle life and low Coulombic efficiency (CE).^{8–11}

The SEI layer formed on the LMA surface from the reduction of solvent and Li salt, incorporating both organic and inorganic species, could stabilize the LMA by minimizing the contact and parasitic side reactions with the electrolyte. Organic-rich SEI layer involving RCO₂Li, however, suffers from a huge volume change of LMA during Li plating/stripping originating from its strong interaction with the LMA surface and low interfacial energy,¹²

THE BIGGER PICTURE

The advance of high-energy-density Li metal batteries (LMBs) is limited by Li dendrite formation, unstable interface, and low Coulombic efficiency (CE). In this direction, electrolyte engineering is essential to optimize the interface formation and realize stable cycling. Localized high-concentration electrolytes, which involve the formation of high-concentration salt-solvent clusters distributed in non-coordinated diluents, have emerged as promising candidates. In this study, we present a new electrolyte family based on the concept of weak-coordinated diluent (WCD) and demonstrated the impact of the molecular structure of the WCD on the electrolyte solvation structure, formation of smaller solvent-salt clusters, and faster anion desolvation kinetics to form ultra-high Li₂O content in the solid electrolyte interphase layer and to realize high CE above 99.5%. These findings guide the design of new electrolytes based on weakly coordinating diluents to further advance the development of LMBs.



leading to unavoidable cracks on the surface during cycling and decreasing the CE. In stark contrast, weak interaction of inorganic SEI components (LiF , Li_2O , and Li_3N) with the LMA surface, their high Young's modulus, and high interfacial energy have been shown to effectively suppress the Li dendrite propagation and boost the Li ion diffusion.¹² Carbonate electrolytes have been successfully applied in conventional LIBs due to the compatibility of organic-rich SEI with graphite anode with a small volume change ($\sim 13\%$) during (de)intercalation.¹³ However, when paired with LMA, the low CE ($< 90\%$) and Li filament formation were normally observed with the carbonate electrolytes owing to the formation of porous, thick and fragile SEI layer, with low shear modulus below 1 GPa, owing to the presence of large amount of organic species such as Li alkyl carbonate (ROCO_2Li) from solvent reduction.^{14,15} In this direction, tuning the composition, thickness and mechanical properties of SEI layer is critical. The additives including ionic liquids,¹⁶ fluoroethylene carbonate (FEC),¹⁷ vinylene carbonate (VC),¹⁸ and amide derivatives¹⁹ have been successfully investigated to improve the CE stability in the carbonate electrolytes by promoting the formation of inorganic-rich SEI layer bearing LiF , Li_2CO_3 , and Li_3N species, but the organic byproducts originating from the decomposition of additives still present a problem. In comparison with the carbonate-based electrolytes, ether-based ones are more stable and compatible toward LMA and promote the formation of chunky and less-dendritic Li.²⁰ The application of ether-based electrolytes in high-voltage LMBs, however, are limited by their low anodic stability (< 4 V). Although the improved CEs are generally obtained, it is still difficult to maintain stability during long cycles owing to the formation of organic lithium alkoxy (ROLi) species on the Li metal surface.²¹ In order to optimize the composition of the SEI layer and to improve the CE stability, LiNO_3 was successfully introduced into ether electrolytes as its decomposition products involve inorganic compounds such as LiN_xO_y , Li_3N , and Li_2O .^{22–24} In addition, tuning the solvation sheath of solvents by controlling their chemical structure and Li^+ solvation power has also emerged as a powerful strategy to promote the formation of an anion-derived inorganic-rich SEI layer.^{25–27} More recently, dual solvent electrolytes including fluorinated 1,6-dimethoxyhexane and 1,2-dimethoxyethane (DME) also showed excellent performance.²⁸ Specifically, high-concentration electrolytes (HCEs) form so-called solvent-in-salt structures by promoting the formation of contact-ion-pair (CIP) and aggregate (AGG) clusters and simultaneously decreasing free solvent molecules, which facilitate the preferential decomposition of anions to form inorganic species in the SEI and increase the oxidation tolerance of ethers markedly.^{14,29–31} HCEs, however, significantly increase the cell cost and also suffer from high viscosity and poor wettability. In this direction, localized HCEs (LHCEs), bearing non-coordinated diluents (NCDs), based on fluorinated ethers were introduced to maintain solvent-in-salt structure through the formation of high-concentration clusters surrounded by diluent molecules at moderate salt concentrations.^{30,32–35} Notably, the chemical structure of the diluents, primarily fluorinated ether-based ones due to their compatibility toward Li metal,³⁴ and their interaction with the clusters and the solvation structure have a profound impact on the composition of SEI. Although inorganic-rich SEI is more favorable compared with the organic one, the properties of SEI also depend strongly on the chemical composition, formation process, crystallinity, nanoscale structure, and morphology. Monolithic/amorphous and uneven SEI morphologies have been observed for LHCEs. Aside from morphology, the composition of SEI also plays a critical role. Unlike HCEs, which show higher LiF content in the SEI, LHCEs exhibit higher Li_2O content as also verified by cryogenic electron microscopy (cryo-EM) analysis, leading to higher CEs and better electrochemical performance.^{36–38} More importantly, the high ionic conductivity and mechanical strength with high elastic modulus (108 GPa) of Li_2O could homogenize electric field distribution and effectively suppress Li dendrite growth.³⁹ Moreover, higher Li + O content in the SEI is expected to have a positive impact on the CE values owing to the

¹Department of Chemistry, University of Fribourg, Chemin de Musee 9, Fribourg 1700, Switzerland

²Laboratory for Joining Technologies and Corrosion, Swiss Federal Laboratories for Materials Science and Technology, Empa, Überlandstrasse 129, Dübendorf CH 8600, Switzerland

³South China Advanced Institute for Soft Matter Science and Technology, School of Emergent Soft Matter, Guangdong Provincial Key Laboratory of Functional and Intelligent Hybrid Materials and Devices, South China University of Technology, Guangzhou 510640, China

⁴School of Chemical and Biological Engineering, Department of Materials Science and Engineering, and Institute of Chemical Processes, Seoul National University, 1 Gwanak-ro, Gwanak-gu, Seoul 08826, Republic of Korea

⁵These authors contributed equally

⁶Lead contact

*Correspondence:
jangwookchoi@snu.ac.kr (J.W.C.),
ali.coskun@unifr.ch (A.C.)

<https://doi.org/10.1016/j.chempr.2022.12.005>

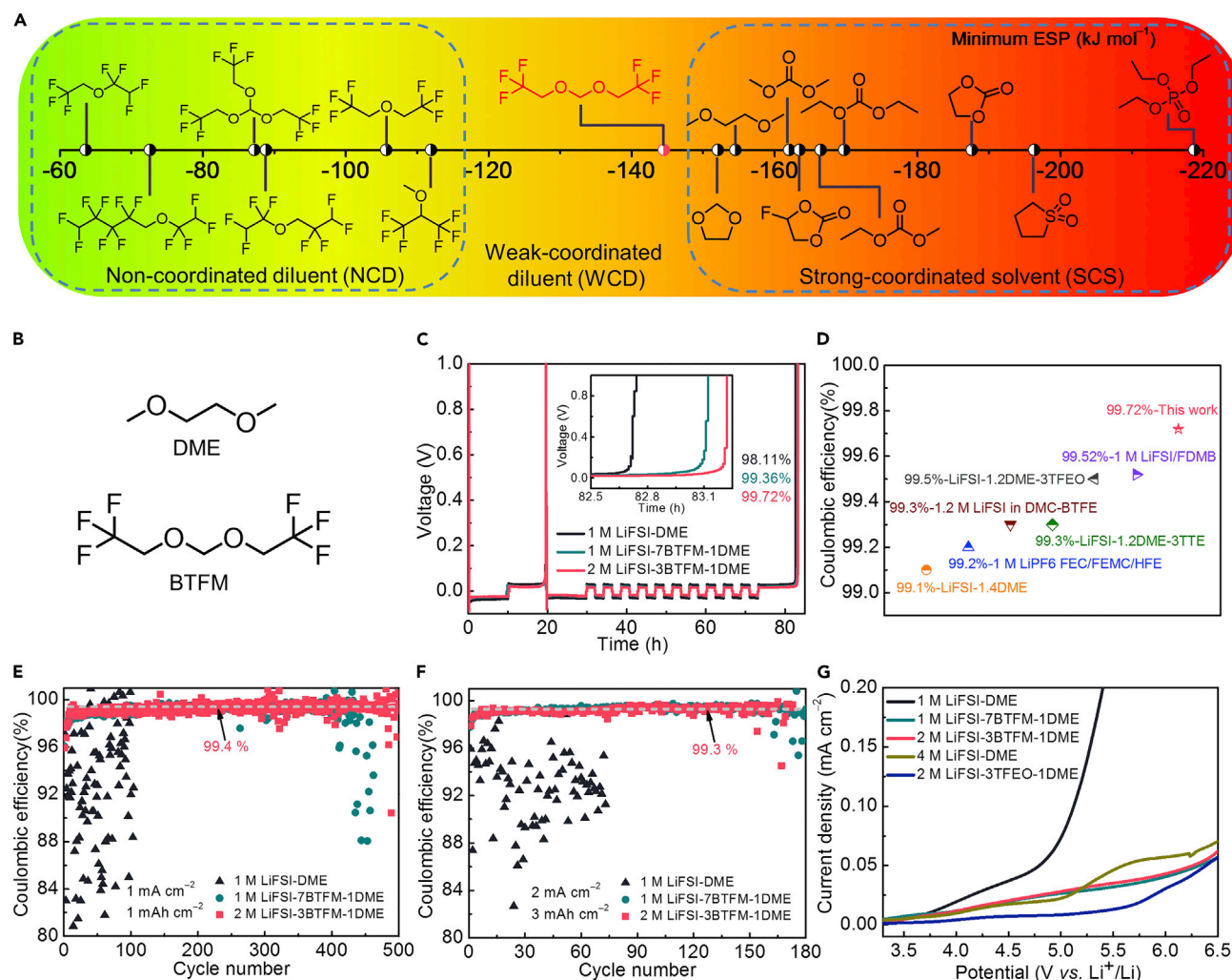


Figure 1. Electrolyte structure and electrochemical performance

(A) Calculated minimum electrostatic potentials (ESPs) of reported diluents and solvents (see also Table S1).

(B) Chemical structures of DME and BTM solvents.

(C) Average CE test of three electrolytes by the standard Aurbach method.⁴⁰

(D) CE value comparisons with previous reports.^{26,30,32,41–43}

(E and F) Cycling measurements of Li|Cu half cells with three electrolytes at the current density and cutoff capacity of 1 mA cm^{-2} and 1 mAh cm^{-2} (E) and 2 mA cm^{-2} and 3 mAh cm^{-2} (F).

(G) Oxidation tolerance of different electrolytes in Li|Al half cells measured by LSV.

abovementioned properties. Upon reviewing previously reported CE values in Li|Cu half cells, it became evident that the CE values had reached a plateau at about 99.5%,^{12,26,32} which is still far below the target of 99.9% for anode-free LMBs. In LHCEs, the diluents surrounding high-concentration clusters could accelerate or slow down the anion decomposition. We reasoned that the minimum electrostatic potential (ESP) value of diluents could play a pivotal role to tune solvation structure of aggregate clusters and anion decomposition kinetics at the Li metal surface to achieve uniformly distributed, high Li_2O content in the SEI to further increase the CE value beyond 99.5%. In this direction, the minimum ESP values of reported solvents and ether-based diluents were first calculated and classified (Figure 1A; Table S1). The traditional ether-based diluents with high minimum ESP value ($>-120 \text{ kJ mol}^{-1}$) are defined as the NCD, whereas the solvents showing low minimum ESP value ($<-150 \text{ kJ mol}^{-1}$) are classified as

strong-coordinated solvent (SCS). We defined the ESP range between NCD and SCS as weak-coordinated diluent (WCD), which is yet to be explored and requires further investigation. Having noted that all the previously reported LHCEs involve NCDs, here we show, for the first time, the critical role of WCD to achieve optimal anion decomposition for homogeneously distributed, high Li_2O content in the SEI to achieve high CE beyond 99.5%. In this direction, we synthesized a fluorinated ether bis(2,2,2-trifluoroethoxy) methane (BTfM) as a WCD and paired it with DME to employ as a solvent mixture (Figure 1B). After dissolving 1 M and 2 M lithium bis(fluorosulfonyl)imide (LiFSI) in BTfM and DME at the volume ratio of 7:1 and 3:1 (referred to as 1 M LiFSI-7BTfM-1DME and 2 M LiFSI-3BTfM-1DME), both electrolytes exhibited excellent oxidation tolerance up to 5.5 V. Specifically, 2 M LiFSI-3BTfM-1DME electrolyte enabled the formation of an inorganic-rich SEI with ultra-high Li_2O content, enabling the highest reported average CE of 99.72% in the Li|Cu half-cell. Moreover, Li|NCM811 ($\text{LiNi}_{0.8}\text{Co}_{0.1}\text{Mn}_{0.1}\text{O}_2$) full cell involving 2 M LiFSI-3BTfM-1DME electrolyte with the N/P (negative/positive capacity) ratio of 2.5 exhibited exceptional electrochemical performance, showing 90% capacity retention after 200 cycles at 1 C and 80% capacity retention after 596 cycles at 3 C, and anode-free Cu|NCM811 full cell maintained 64% retention after 80 cycles at 1 C ($1\text{ C} = 1.6\text{ mA cm}^{-2}$, $1\text{ C} = 200\text{ mA g}^{-1}$).

RESULTS

Electrolyte design and characterization

From the molecular design perspective, acetal functional group, $\text{O}-\text{CH}_2-\text{O}$, was introduced due to its lower Li^+ affinity compared with $\text{O}-\text{CH}_2-\text{CH}_2-\text{O}$ by stereoelectronic effects.⁴⁴ Moreover, the introduction of electron-withdrawing group ($-\text{CF}_3$) not only increased the high-voltage tolerance but also decreased the solvation power to achieve WCD. BTfM (Figure 1B) was synthesized from paraformaldehyde and 2,2,2-trifluoroethanol in a single step reaction at room temperature with 37% yield. The formation of BTfM was verified by nuclear magnetic resonance (NMR) spectroscopy analysis as shown in Figures S1–S3. In order to explore the influence of the salt concentration and volume ratio of BTfM on the SEI components, 1 M LiFSI-7BTfM-1DME and 2 M LiFSI-3BTfM-1DME electrolytes were prepared based on the equal molar ratio of Li salt to DME to have a similar inner solvation sheath in both electrolytes. Compared with the recently reported approach²⁸ using dual-solvents, where both solvents can dissolve the salt, BTfM cannot dissolve the salt (Figures S4–S6) but can tune the solvation structure by partially participating in the first solvation sheath along with DME. 1 M LiFSI salt dissolved in DME (referred to as 1 M LiFSI-DME) was used as a control electrolyte. The physical properties of each solvent and electrolyte are listed in Tables S2 and S3. The ionic conductivities of 1 M LiFSI-DME, 1 M LiFSI-7BTfM-1DME, and 2 M LiFSI-3BTfM-1DME were found to be 22.5, 2.7, and 5.5 mS cm^{-1} , respectively. In order to evaluate the compatibility of electrolytes with LMA, average CE values were monitored by the standard Aurbach method⁴⁰ in Li|Cu half cells. The cell with 1 M LiFSI-DME obtained the average CE value of only 98.11 %. HCE, 4 M LiFSI dissolved in DME (referred to as 4 M LiFSI-DME), exhibited average CE of 98.68 % (Figure S7). In stark contrast, the cells with BTfM co-solvent exhibited much improved average CE values of 99.36% (1 M LiFSI-7BTfM-1DME) and 99.72% (2 M LiFSI-3BTfM-1DME), which is, to the best of our knowledge, the highest value reported to date (Figures 1C and 1D) with good reproducibility (Figure S8). Furthermore, long cycling tests of Li|Cu half cells with different electrolytes were carried out to reveal the CE stability. At a current density of 1 mA cm^{-2} and cutoff capacity of 1 mAh cm^{-2} , the cell with 1 M LiFSI-DME showed a serious fluctuation of CE due to the unstable SEI layer formation (Figure 1E), and the one with 4 M LiFSI-DME also showed low stability and CE value less than 98%

within 100 cycles (Figure S9). In comparison, cells using 1 M LiFSI-7BTfM-1DME and 2 M LiFSI-3BTfM-1DME electrolytes showed a rather stable CE of 99.4% within 400 and 500 cycles, respectively. The related charge-discharge profiles confirmed that the CE difference compared with the control samples was influenced by the stripping capacity, an indication for alleviating plated Li consumption and “dead” Li formation (Figure S10). Li|Cu half cells were also cycled under harsh conditions at the current density of 2 mA cm^{-2} and a cutoff capacity of 3 mAh cm^{-2} . The cell with 1 M LiFSI-DME showed CE value less than 97% with obvious oscillation. In contrast, average CE of 99.3% was observed in both BTfM-based electrolytes within 170 cycles (Figure 1F). Moreover, a high current density of 5 mA cm^{-2} with a cutoff capacity of 1 mAh cm^{-2} was applied to evaluate BTfM-based electrolytes under even tougher conditions (Figure S11 and Table S4 for performance comparison). Although the cell with 2 M LiFSI-3BTfM-1DME exhibited a stable CE of 98.3% for 110 cycles, the one with 1 M LiFSI-7BTfM-1DME only stabilized for 15 cycles. Average CE of long cycling was also evaluated by the Li|Li cells⁴⁵ at a different current density as shown in Figure S12. Interfacial stability and polarization were also probed by using Li|Li symmetrical cells with different electrolytes at the current density of 1 mA cm^{-2} and cutoff capacity of 1 mAh cm^{-2} (Figure S13). The cells with 1 M LiFSI-DME, 1 M LiFSI-7BTfM-1DME, and 2 M LiFSI-3BTfM-1DME electrolytes survived for 600, 1,400, and 1,100 h, respectively, followed by a sharp increase in the overpotential. The slightly inferior performance of 2 M LiFSI-3BTfM-1DME compared with its 1 M LiFSI-7BTfM-1DME counterpart originated presumably from the higher salt concentration of 2 M LiFSI-3BTfM-1DME.^{46,47} Cyclic voltammetry (CV) of Li|Cu half cells with different electrolytes also revealed the high interfacial stability of BTfM-based electrolytes derived from overlapping curves (Figure S14). Oxidation stability of electrolytes is highly important to be compatible with state-of-the-art commercial Ni-rich cathodes. Accordingly, linear sweep voltammetry (LSV) was conducted in Li|Al half cells with different electrolytes (Figure 1G). In contrast with the low oxidation stability ($<4 \text{ V}$) of 1 M LiFSI-DME, BTfM-based electrolytes showed higher oxidation stability up to 5.5 V, ascribed to (1) the lower HOMO energy level of BTfM (-8.28 eV) compared with DME (-7.19 eV) by the introduction of electron-withdrawing $-\text{CF}_3$ group (Figure S15), (2) reduced free DME molecules, and (3) downward shift of the HOMO energy of coordinated DME in the aggregate cluster.³⁵ The improved oxidative stability of the BTfM-based electrolytes was also proved by their anti-corrosion capability on Al electrodes (Figures S16–S19). These results clearly show the potential of BTfM-based electrolytes in terms of their compatibility with both LMA and a high-voltage cathode.

Li metal morphology

As the CE performance is closely related to Li plating, scanning electron microscopy (SEM) analysis was conducted to demonstrate the influence of different electrolytes on the morphology of plated Li (Figure 2). First, Li capacity of 3 mAh cm^{-2} was plated on Cu foil at the current density of 2 mA cm^{-2} with different electrolytes. The plated Li with 1 M LiFSI-DME showed several cracks, Li filaments, and bare Cu substrate, which revealed the non-uniform coverage of Li plating and continuous, undesirable side reactions with electrolyte (Figure 2A). In contrast, the plated Li with 1 M LiFSI-7BTfM-1DME showed uniform distribution of chunky Li with small gaps (Figure 2B). In the case of 2 M LiFSI-3BTfM-1DME electrolyte, the plating morphology was superior owing to its flatness, larger Li grains, smaller specific area, and less cracks, which decrease the contact and side reactions between Li metal and electrolyte (Figure 2C). After 20 cycles, the same amount of Li (3 mAh cm^{-2}) was plated on Cu foil again at a constant current density of 2 mA cm^{-2} with different electrolytes to

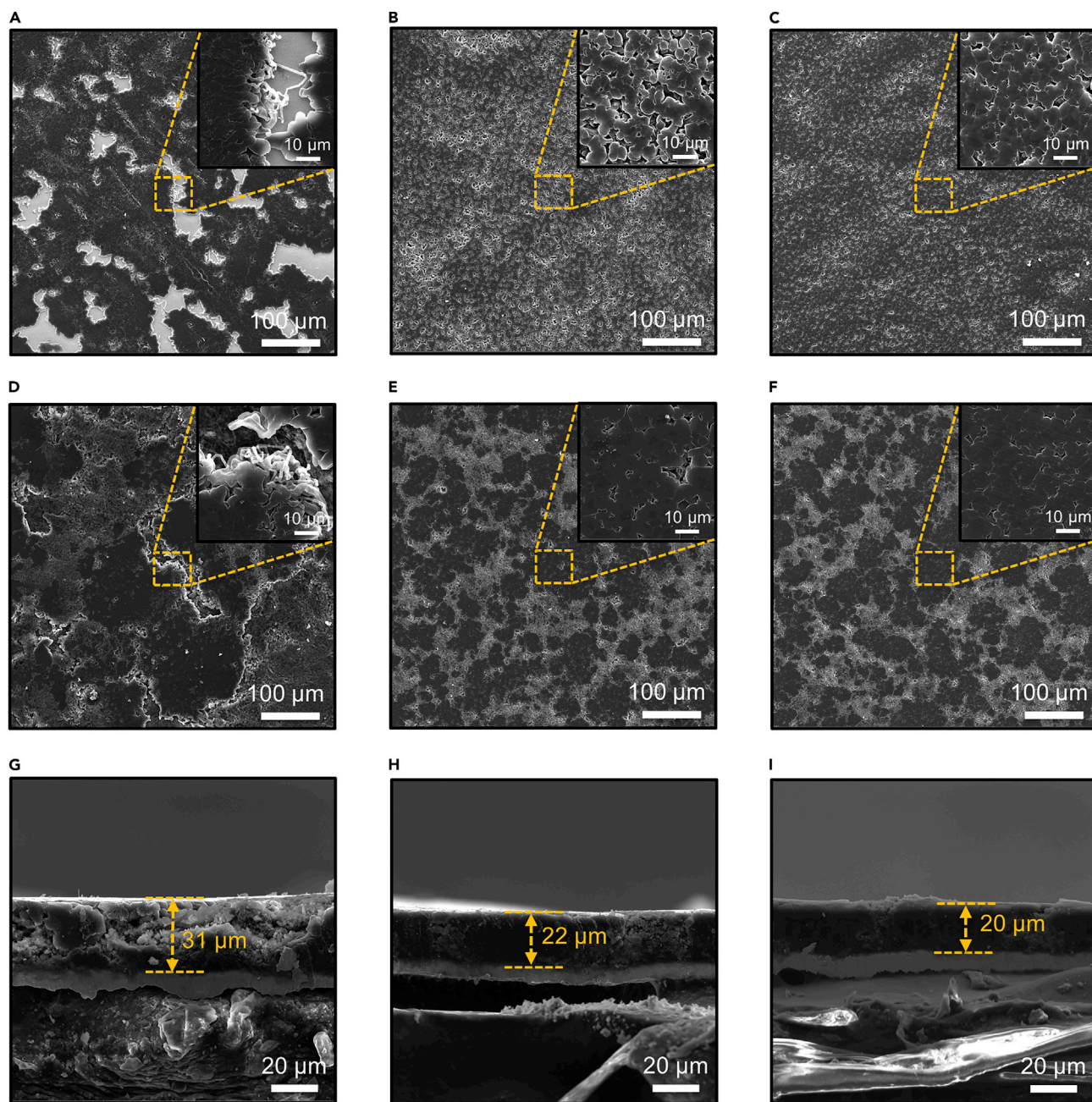


Figure 2. Li plating morphology

(A–C) SEM images of the Li plating morphology on Cu foil after one cycle in 1 M LiFSI-DME (A), 1 M LiFSI-7BTfM-1DME (B), and 2 M LiFSI-3BTfM-1DME (C) electrolytes.

(D–F) SEM images of the Li plating morphology on Cu foil after 20 cycles in 1 M LiFSI-DME (D), 1 M LiFSI-7BTfM-1DME (E), and 2 M LiFSI-3BTfM-1DME (F) electrolytes.

(G–I) Cross-sectional SEM images of plated Li on Cu foil after 20 cycles in 1 M LiFSI-DME (G), 1 M LiFSI-7BTfM-1DME (H), and 2 M LiFSI-3BTfM-1DME (I) electrolytes.

Insets are zoom-in images. All Li|Cu half cells were cycled at a current density of 2 mA cm^{-2} with a cutoff capacity of 3 mAh cm^{-2} .

monitor Li morphology evolution. The plated Li with 1 M LiFSI-DME displayed a rough surface, a large number of cracks, Li dendrites, loose packing, and a thick deposition layer of $31 \mu\text{m}$ (Figures 2D and 2G) owing to the repeated rupture and formation of fragile SEI during cycling, which is linked to serious CE fluctuation

(Figures 1E and 1F). On the contrary, the plated Li with 1 M LiFSI-7BTFM-1DME showed a flat surface, uniform distribution of Li, and accumulated SEI, the corresponding deposition Li with a thickness of 22 μm (Figures 2E and 2H). Moreover, larger Li grains with fewer holes and less accumulated SEI were obtained when using 2 M LiFSI-3BTFM-1DME electrolyte along with a thinner Li anode of 20 μm (Figures 2F and 2I). Additional SEM images and error bars for Figures 2G–2I are provided as shown in Figures S20 and S21. These results clearly show the profound impact of electrolyte design on the Li plating morphology and thickness.

Performance of Li metal batteries

Based on the excellent Li metal half-cell performance and high-voltage stability, BTFM-based electrolytes were further evaluated in little-excess Li|NCM811 full cells and anode-free Cu|NCM811 full cells. The cycling performances of Li|NCM811 full cells (N/P ratio of 2.5) with different electrolytes at 1 C are shown in Figure 3A. Two commercial carbonate electrolytes, 1 M lithium hexafluorophosphate (LiPF_6) in ethylene carbonate (EC)/ethyl methyl carbonate (EMC) by the volume ratio of 1:1 (referred to as 1 M LiPF_6 -EC-EMC) and 1 M LiPF_6 in EC/EMC/dimethyl carbonate (DMC) by the volume ratio of 1:1:1 with 2 wt % VC (referred to as 1 M LiPF_6 -EC-EMC-DMC-2 wt % VC), were also evaluated for comparison under the same conditions. The full cell capacity based on 1 M LiPF_6 -EC-EMC showed continuous fading before 55 cycles and then drastically dropped down to 31 mAh g^{-1} at the 70th cycle due to the formation of a porous SEI, dead Li, and electrolyte consumption by side reactions. When using 1 M LiPF_6 -EC-EMC-DMC-2 wt % VC electrolyte, the full cell capacity stabilized within 57 cycles due to the Li anode protection through VC polymerization, yet markedly decreased to 14.5 mAh g^{-1} at the 72th cycle stemming from the electrolyte consumption, interfacial resistance, and accumulated SEI.³² Due to the low-voltage stability of 1 M LiFSI-DME, the related full cell survived only for 19 cycles. With HCE, 4 M LiFSI-DME, the capacity of full cell merely kept stable for 50 cycles owing to the high viscosity and unfavorable CE (Figure S22). By stark contrast, the performance of Li|NCM811 full cells was substantially improved with BTFM-based electrolytes. The capacity of cell with 1 M LiFSI-7BTFM-1DME remained 125.9 mAh g^{-1} after 150 cycles with the capacity retention value of 81%, which also showed good reproducibility (Figure S23). Furthermore, the full cell using 2 M LiFSI-3BTFM-1DME exhibited the best cycling stability with 147.4 mAh g^{-1} capacity and 90% retention after 200 cycles, also further verified by the excellent reproducibility data (Figure S24). These results agree nicely with the CE results, which points to the fact that Li metal protection through electrolyte engineering plays a pivotal role in little-excess Li metal full cells. Charge-discharge profiles of full cells with different electrolytes were also compared (Figures 3B–3D and S25). The polarization increase in the carbonate-based electrolyte originated from the continual electrolyte depletion and repeated SEI formation by the side reactions during cycling. The oxidation instability of DME-based electrolytes restrained long cycling of high-voltage LMBs as evidenced by the charging profile that was not able to reach the cut-off potential. Differently, the polarization in the full cells with BTFM-based electrolytes remained steady during long cycling owing to Li metal stabilization, robust SEI formation, and high-voltage stability. Furthermore, Li|NCM811 full cells (N/P ratio of 2.5) with BTFM-based electrolytes were also tested at 3 C (4.8 mA cm^{-2}) as shown in Figure 3E. Taking 80% capacity retention as the benchmark, full cell with 2 M LiFSI-3BTFM-1DME cycled 596 cycles, whereas the one with 1 M LiFSI-7BTFM-1DME was stable for only 47 cycles. The obvious difference in cycling performance at high rate fitted well with the CE test at high current density (5 mA cm^{-2}) in Li|Cu half cells (Figure S11). Electrochemical impedance spectroscopy (EIS) analysis was also conducted to compare the interfacial resistance (R_i) in full cells with different

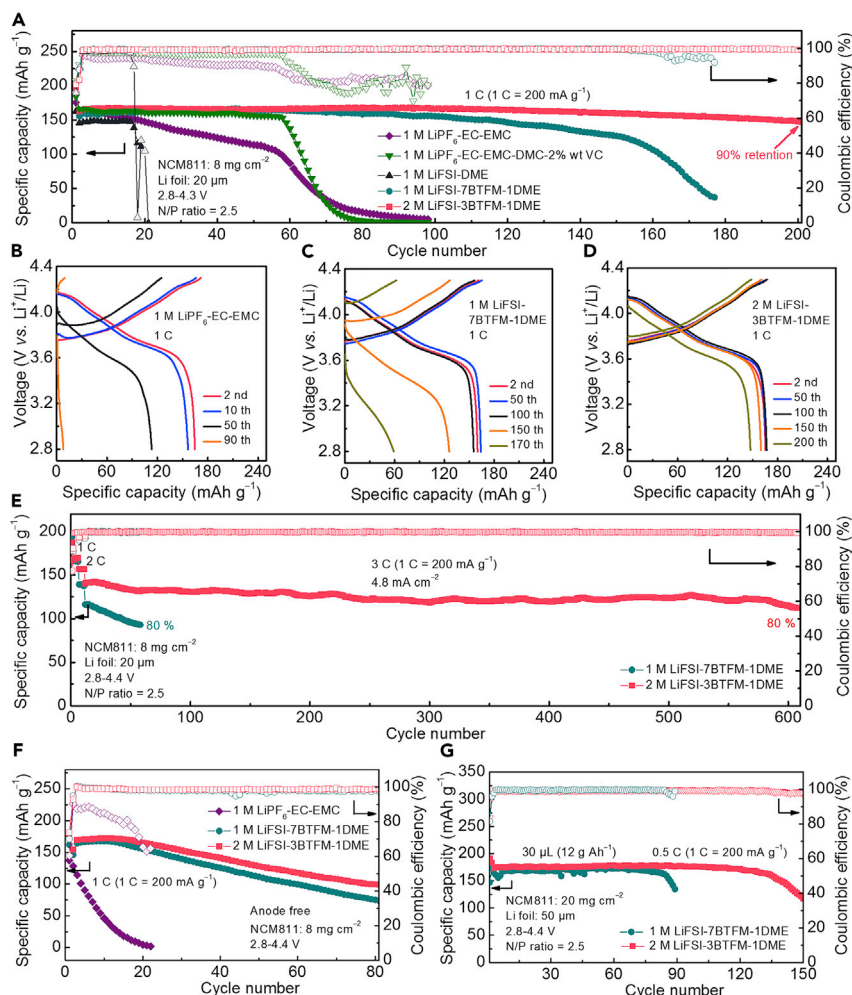


Figure 3. Electrochemical performance of full cells

(A) Cycling performance of Li|NCM811 full cells with different electrolytes at 1 C after the first formation cycle at 0.1 C.
(B–D) Charge-discharge profiles of Li|NCM811 full cells at different cycles with 1 M LiPF₆-EC-EMC (B), 1 M LiFSI-7BTFM-1DME (C), and 2 M LiFSI-3BTFM-1DME (D) electrolytes.
(E) Cycling performance of Li|NCM811 full cells with BTFM-based electrolytes at 3 C after formation cycles (0.1 C, 1 cycle; 1 C, 5 cycles; and 2 C, 5 cycles).
(F) Cycling performance of anode-free Cu|NCM811 full cells with different electrolytes at 1 C after first formation cycle at 0.1 C.
(G) Cycling performance of high loading Li|NCM811 full cells at 0.5 C by E/C ratio of 12 (g Ah⁻¹) and N/P ratio of 2.5.

electrolytes (Figure S26). The smallest R_i (8 Ω) in cell with 2 M LiFSI-3BTFM-1DME proved the stable interface formation after cycling, in contrast to the large R_i values of 30 and 35 Ω using 1 M LiPF₆-EC-EMC and 1 M LiFSI-DME electrolytes, respectively, derived from continual SEI accumulation and electrolyte decomposition. We also tested anode-free Cu|NCM811 full cells with different electrolytes at 1 C between 2.8 and 4.4 V (Figure 3F). The Cu|NCM811 full cell with 1 M LiPF₆-EC-EMC showed a fast capacity fading down to 3 mAh g⁻¹ with only 2% retention after 20 cycles, which reflected the continual consumption of plated Li on Cu foil, originating from low CE due to porous SEI and dead Li formation. Anode-free full cells with 1 M LiFSI-7BTFM-1DME and 2 M LiFSI-3BTFM-1DME electrolytes showed better capacity retention values of 51% and 64% after 80 cycles, respectively, attributed to

the robust SEI formation, controlled Li morphology, and excellent Li metal performance.

Moreover, BTFM-based electrolytes were also subjected to harsh electrochemical conditions. Accordingly, a high loading NCM811 cathode (20 mg cm^{-2}) paired with $20 \text{ }\mu\text{m}$ Li foil (N/P ratio of 1) was evaluated with BTFM-based electrolytes at 0.5 C between 2.8 and 4.4 V (Figure S27). Although the capacity of high loading full cell with $1 \text{ M LiFSI-7BTFM-1DME}$ remained at 152.5 mAh g^{-1} after 100 cycles with 90% capacity retention, the one with $2 \text{ M LiFSI-3BTFM-1DME}$ electrolyte showed a capacity of 140.2 mAh g^{-1} after 75 cycles with 82% retention and both cells exhibited good reproducibility (Figures S28 and S29). For the $2 \text{ M LiFSI-3BTFM-1DME}$ electrolyte, the opposite trend in electrochemical performance of the high loading full cells compared with the lower loading ones with the same Li foil ($20 \text{ }\mu\text{m}$) could be explained by Li anode failure (Figure S30), in agreement with results of Li|Li symmetrical cells in Figure S13, but not the cathode as both cells exhibited similar CEI compositions (Figure S31). Li foil ($50 \text{ }\mu\text{m}$) paired with NCM811 cathode by the N/P ratio of 2.5 was further tested (Figure 3G). Under these conditions, the full cell using $2 \text{ M LiFSI-3BTFM-1DME}$ retained 81% of the original capacity after 143 cycles, whereas the cell with $1 \text{ M LiFSI-7BTFM-1DME}$ showed 82% retention after 89 cycles with good reproducibility (Figure S32). The related charge-discharge profiles of $2 \text{ M LiFSI-3BTFM-1DME}$ electrolyte are displayed in Figure S33. The various rate capability of high loading full cells was tested at the constant charge rate of 0.5 C (Figure S34). The discharge capacity of full cell with $2 \text{ M LiFSI-3BTFM-1DME}$ was 173 mAh g^{-1} at 2 C (8 mA cm^{-2}), but only 149 mAh g^{-1} with $1 \text{ M LiFSI-7BTFM-1DME}$ when tested at the same conditions. High loading full cells under lean electrolyte conditions were also evaluated as shown in Figure S32.

Interface characterization

In order to explain the excellent performance of the BTFM-based electrolytes, X-ray photoelectron spectroscopy (XPS) analysis was conducted to probe the SEI and CEI compositions in Li|NCM811 full cells after 30 cycles at 1 C . Figures 4A, 4D, 4G, and 4J show the XPS sputter-depth profiles of the average elemental concentrations of Li, P, N, O, S, F, and C (in atomic percent) in the SEI layers (up to a sputter depth of roughly $12 \text{ min} \times 2.3 \text{ nm/min} \approx 28 \text{ nm}$; see material characterizations in supplemental information). Clearly, the highest C concentration in the interior of the SEI layer ($>10 \text{ atom } \%$) was observed for the $1 \text{ M LiPF}_6\text{-EC-EMC}$ electrolyte. The C content strongly increased toward the SEI surface, which indicated that the $1 \text{ M LiPF}_6\text{-EC-EMC}$ SEI layer was enriched in organic species at its outer surface. The C content in the SEI layer (and at its surface) was considerably lower ($<5 \text{ atom } \%$) for the BTFM-based electrolytes. This result suggested that the SEI layers of the BTFM-based electrolytes were much more homogeneous in their composition and had a significantly higher content of inorganic species. Preferential incorporation of inorganic species during cycling should be accompanied with relatively high Li contents within the SEI layer. For the $1 \text{ M LiPF}_6\text{-EC-EMC}$ SEI layer, the Li content increased with increasing depth from about 22% to 43%, which confirmed the rather heterogeneous incorporation of inorganic species during cycling, leading to a relatively unstable CE of the Li anode. Analogously, the Li content in the 1 M LiFSI-DME electrolyte SEI layer steadily increased with increasing sputter depth from about 34% to 51% indicating the non-uniform distribution of inorganic species. On the contrary, the Li content in the SEI layers formed from the BTFM-based electrolytes initially increased with increasing sputter depth but reached an approximately constant value after 4 min of sputtering (i.e. 47% for $1 \text{ M LiFSI-7BTFM-1DME}$ and 57% for $2 \text{ M LiFSI-3BTFM-1DME}$); this is a clear indication of the formation of more uniform and inorganic-rich SEI layers in the BTFM-based electrolytes.

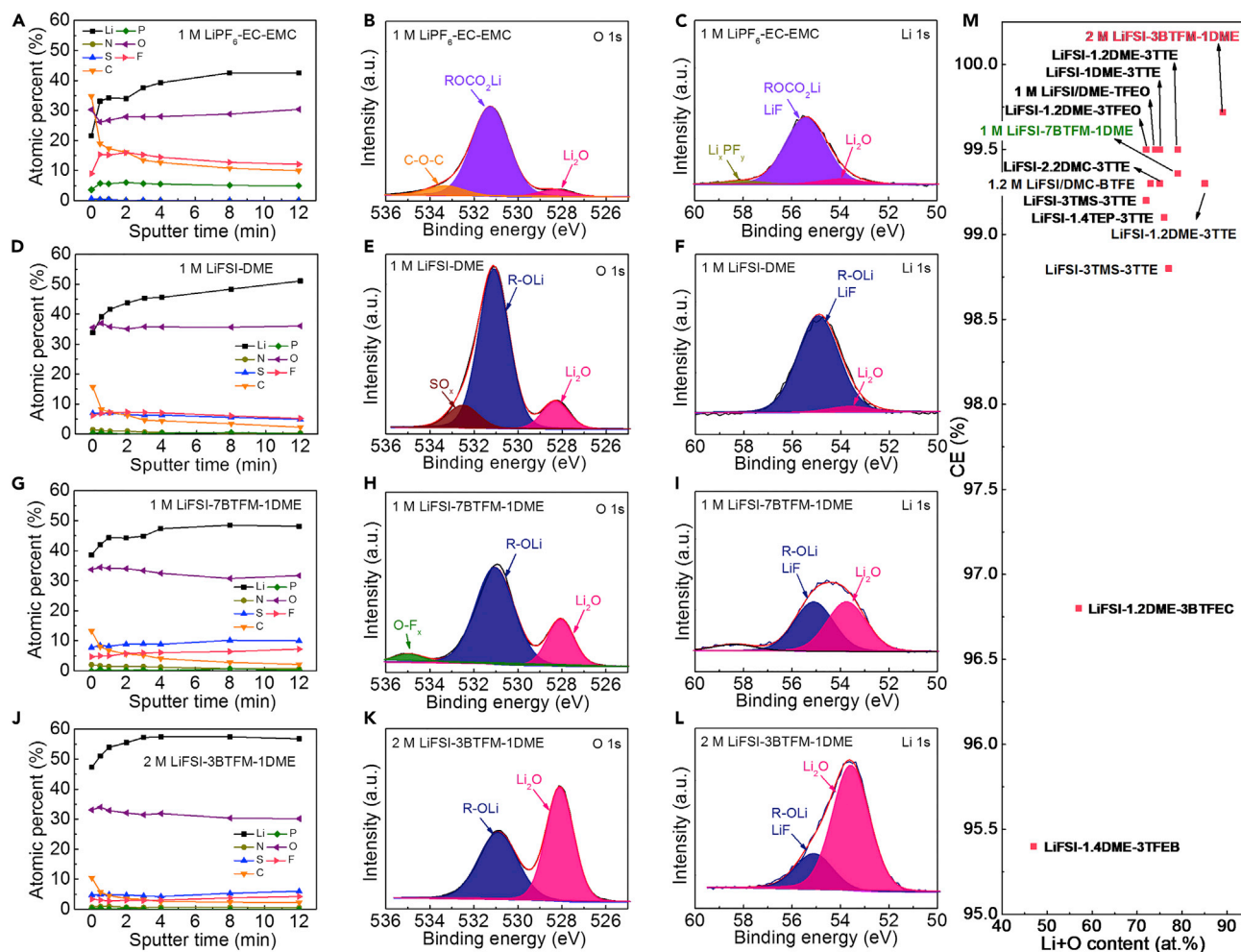


Figure 4. XPS analyses of the SEI layers on the Li metal anode surface in the Li|NCM811 full cells

(A, D, G, and J) Elemental sputter-depth profiles of the anode SEI layers in the Li|NCM811 full cells for 1 M LiPF₆-EC-EMC (A), 1 M LiFSI-DME (D), 1 M LiFSI-7BTfM-1DME (G), and 2 M LiFSI-3BTfM-1DME (J) electrolytes.

(B, E, H, and K) Resolved chemical species in the O 1s spectra of the SEI layers after 1 min sputtering for 1 M LiPF₆-EC-EMC (B), 1 M LiFSI-DME (E), 1 M LiFSI-7BTfM-1DME (H), and 2 M LiFSI-3BTfM-1DME (K) electrolytes.

(C, F, I, and L) Resolved chemical species in the Li 1s spectra of the anode SEI layers after 1 min sputtering for 1 M LiPF₆-EC-EMC (C), 1 M LiFSI-DME (F), 1 M LiFSI-7BTfM-1DME (I), and 2 M LiFSI-3BTfM-1DME (L) electrolytes. Prior to the XPS characterization, all Li|NCM811 full cells were cycled at 1 C for 30 cycles.

(M) CE values and Li + O atomic content in the SEI layer are based on BTfMs and previously reported electrolytes^{30,32–35,43}; the data were also summarized in Table S5.

Figure 4M evidenced a possible trend between the Li + O content in the SEI layer and the CE value; corresponding data for previously reported electrolytes involving NCDs and BTfMs as WCDs (as summarized in the Table S5) are plotted. Notably, the 2 M LiFSI-3BTfM-1DME SEI exhibited the highest Li + O content of 89%, as well as the highest CE value. This result clearly indicated that Li₂O_x chemical species play a pivotal role for obtaining the record-high CE of 99.72% of the 2 M LiFSI-3BTfM-1DME electrolyte (Figure 1C). The elemental concentrations in the sputter-depth profiles gave no detailed information on the chemical binding states of Li, O, C, F, N, and S in the SEI layers. The chemical constitution of each SEI layer was revealed from the spectral reconstructions of the measured Li 1s, O 1s, C 1s, F 1s, N 1s, and S 2p spectra, as shown for a representative sputter time of 1 min for the C 1s, F 1s, N 1s, and S 2p spectra in the Figures S35–S39. The presence of Li₂O in the SEI layers was revealed from the spectral

deconvolutions of the O 1s and Li 1s spectra, as measured after a sputtering time of 1 min, as shown in Figures 4B, 4C, 4E, 4F, 4H, 4I, 4K, and 4L, respectively. In addition, the reconstructed Li 1s and O 1s spectra after each sputtering step (from 0 to 12 min) are presented in Figures S40 and S41, respectively. By following the relative spectral contributions of the resolved Li 1s and O 1s species with increasing sputter depth (Figures S40 and S41), the organic ROCO₂Li content in the 1 M LiPF₆-EC-EMC and organic ROLi in the 1 M LiFSI-DME SEI layers were significantly higher than the inorganic Li₂O content, which suggests a rather heterogeneous incorporation of inorganic and organic species. In the case of BTFM-based electrolytes, however, the Li₂O-to-ROLi atomic ratio remained approximately constant across the sputter depth (Figures S40C, S40D, S41C, and S41D), which clearly evidenced that the SEI layers from the BTFM-based electrolytes were rather homogeneous in composition and relatively rich in inorganic species, as attributed to the preferential fast decomposition of FSI anions along with the suppressed side reactions of DME. As indicated by the comparison of the reconstructed S 2p spectra of the DME-based SEI layers after 1 min sputtering (Figure S39), the SO₂F-to-S²⁻ atomic ratio was the lowest for the 2 M LiFSI-3BTFM-1DME electrolyte, which also indicated a more efficient decomposition of Li salt in the 2 M LiFSI-3BTFM-1DME electrolyte (compared with the 1 M LiFSI-7BTFM-1DME and 1 M LiFSI-DME electrolytes).³² Besides the concentration-depth profiles of each element (see Figure 4), the corresponding concentration-depth profiles of each chemical species (for each element) are given in the Figures S42 and S43, where SEI in 2 M LiFSI-3BTFM-1DME showed Li₂O content up to 63%. As evidenced by the depth-resolved chemical constitution of the different SEI layers, BTFM-based electrolytes enabled three key features for the SEI layer to achieve ultra-high CE value—namely, the formation of a homogeneous, Li₂O-rich, and low-organic-content SEI layer. Cryogenic transmission electron microscopy (cryo-TEM), oxygen mapping, and fast Fourier transform analyses were also conducted to characterize SEI layer of 0.25 mAh cm⁻² Li deposit on carbon film-coated Cu grid at a current density of 0.5 mA cm⁻² using 1 M LiFSI-7BTFM-1DME and 2 M LiFSI-3BTFM-1DME electrolytes (Figure S44). These series of analyses also indicated uniformly distributed elements and rich inorganic components in the SEI layers. The chemical constitutions of the CEI layers formed on the cathodes in the different electrolytes were also analyzed by XPS (Figures S45–S51). It follows that the BTFM-based electrolytes resulted in a relatively lower concentration of C species at the CEI surface (Figure S45) accompanied by a significantly increased LiF surface content (Figure S46), pointing to the formation of a LiF-rich inorganic CEI layer in the BTFM-based electrolytes. As shown in the Figures S52–S54, SEM images of the cathode after cycling showed a relatively flat and dense surface in BTFM-based electrolytes, especially for the 2 M LiFSI-3BTFM-1DME (Figures S53D and S54D), as attributed to the surface protection by the LiF-rich CEI. On the contrary, the cathode in 1 M LiFSI-DME showed irregular surface morphology, which was attributed to strong electrolyte decomposition at a high voltage. Based on the XPS analysis, it can thus be concluded that the excellent performance of full cells with BTFM-based electrolytes was due to the formation of a homogeneous Li₂O-rich SEI layer and a LiF-rich CEI surface. Parasitic reactions on the cathode side in the full cell was evaluated by a kinetic study,^{48,49} BTFM-based electrolyte exhibited limited parasitic reactions at 4.4 V (Figures S55 and S56; Table S6).

Solvation structure

Although the compositions of SEI and CEI were elucidated by XPS analysis, the related formation mechanism by electrolyte decomposition need to be further explored (Figure 5). Raman spectroscopy was first employed to probe the solvation structures in different electrolytes (Figure 5A). Compared with the pure DME solvent, 1 M LiFSI-DME electrolyte exhibited two new peaks at 717 and 875 cm⁻¹ assigned to free FSI

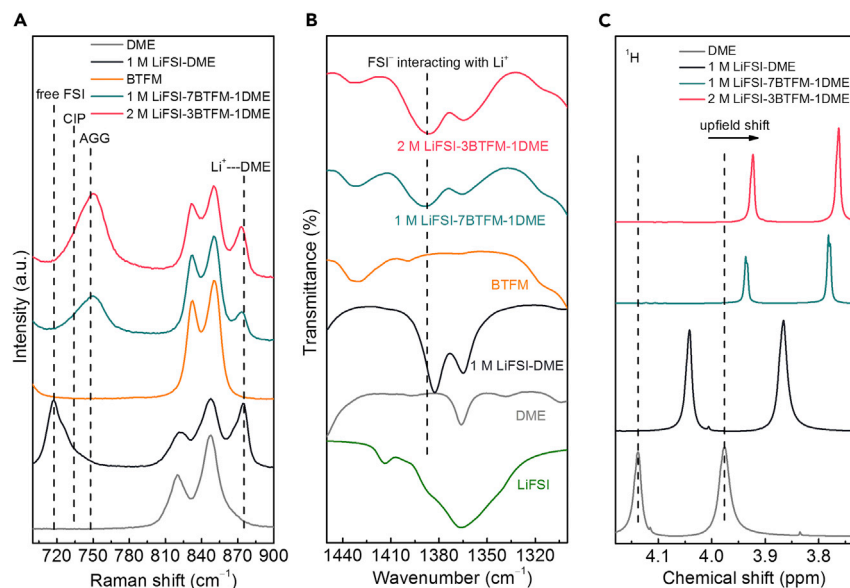


Figure 5. Electrolytes solvation structure

(A) Raman spectra of different solvents and electrolytes.

(B) FTIR spectra of different solvents and electrolytes.

(C) ¹H NMR spectra of different solvents and electrolytes.

anion and coordination of DME to Li⁺, respectively. With the introduction of BTFM, the peak of free FSI anion disappeared, which was accompanied by the appearance of a new peak at 748 cm⁻¹ assigned to aggregate (AGG) solvation structure in the case of the BTFM-based electrolyte reflecting the strong coordination between Li⁺ and FSI anion.⁵⁰ This result is quite significant to show that unlike carbonate-based diluents,³⁴ BTFM as a WCD does not interfere with the formation of high-concentration clusters. Moreover, Fourier transform infrared (FTIR) spectroscopy analysis was performed to compare the solvation structures of different electrolytes (Figures 5B and S57), which also exhibited strong coordination between FSI anion and Li⁺ (1,387 cm⁻¹) along with the disappearance of free DME molecules (1,105 cm⁻¹)²⁶ in the BTFM-based electrolytes. NMR analysis is a powerful tool to probe the nature of the solvation shell in LHCEs. As shown in Figures 5C and S58, the upfield shift in the ¹H NMR spectra going from DME to 1 M LiFSI-DME to 1 M LiFSI-7BTFM-1DME and to 2 M LiFSI-3BTFM-1DME proved the formation of a stronger solvation shell of FSI anion and DME around Li⁺ by the addition of BTFM.⁵¹ In order to analyze the impact of WCD and NCD on the structure of solvation cluster, we also measured the NMR spectrum of tris(2,2,2-trifluoroethyl)orthoformate (TFEO),^{32,34} which is a NCD, under the same electrolyte configuration (2 M LiFSI-3TFEO-1DME). Compared with the 2 M LiFSI-3TFEO-1DME, the downfield shifts of 2 M LiFSI-3BTFM-1DME in its ¹H, ¹⁹F, and ⁷Li NMR spectra clearly indicated the relatively weakened FSI anion-Li⁺ coordination²⁵ by the introduction of WCD (Figure S59) compared with the NCD. Molecular dynamics (MDs) simulation was performed to prove the concept of WCD by the participation of BTFM in the first solvation sheath, although it cannot dissolve the Li salt (Figures S60–S62), consistent with the NMR results (Figure S59C). Moreover, the interactions between the F atoms of FSI anions with the BTFM were predicted to be much weaker compared with the TFEO (Figure S63), which significantly accelerated the rate of desolvation and enhanced anion decomposition kinetics at the Li metal surface promoting the formation of inorganic-rich SEI. TFEO-based electrolyte as control was also compared with BTFM-based electrolyte (Figures S64–S66). Moreover, smaller

solvation cluster size in BTFM-based electrolyte (WCD) was also proven by diffusion ordered spectroscopy (DOSY) NMR (Figure S67) with higher Li^+ diffusion coefficient compared with the TFE0 (NCD). Notably, BTFM as a WCD did not interfere with the formation of aggregate clusters, where one FSI anion is coordinating to two or more Li cations. Increasing the salt concentration from 1 to 2 M also further favored the participation of anions into the solvation shell around Li^+ , thus promoting the formation of an inorganic-rich SEI layer. Critically, slightly weakened FSI anion- Li^+ coordination in the case of WCD relative to NCD while retaining aggregate clusters along with the lower affinity of WCD toward FSI anion appear to be the key parameters to realize the ultra-high Li_2O content and CE values beyond 99.5%, presumably due to the enhanced decomposition kinetics through the decreased desolvation energy of the ions from the clusters with a weaker solvation shell. In order to reveal the specific role of acetal core ($-\text{O}-\text{CH}_2-\text{O}-$) in BTFM, we performed DFT calculations and compared the Li^+ binding modes and binding energies of BTFM, bis(2,2,2-trifluoroethoxy)ethane (BTFE) with a glycol core ($-\text{O}-\text{CH}_2-\text{CH}_2-\text{O}-$), TFE0, and DME (Figure S68). DME (-273.683 kJ/mol) showed the highest binding energy toward Li^+ , which was followed by BTFE (-264.356 kJ/mol), thus highlighting the critical role of $-\text{O}-\text{CH}_2-\text{CH}_2-\text{O}-$ moiety for strong solvation ability.⁵² It should be also noted that both DME and BTFE can dissolve the Li salts. In the case of BTFM (-214.108 kJ/mol), however, we observed much weaker binding compared with BTFE, thus pointing to the impact of the central alkyl moiety in determining the binding mode with Li^+ and verifying the lower Li^+ affinity of acetal core. TFE0 (-204.608 kJ/mol) with the orthoformate core, on the other hand, showed the lowest binding ability. Although the acetal core of BTFM can weaken the Li^+ solvation power, its high electron density enable partial coordination with Li^+ to precisely optimize the solvation cluster in electrolytes. These results clearly show the critical role of solvation structure enabled by WCDs to control the nature, morphology, and homogeneity of SEI, thus forming an inorganic-rich SEI and CEI from the preferential reduction and decomposition of FSI anion during cycling.

DISCUSSION

A class of BTFM-based electrolytes as weakly coordinating diluents was introduced to achieve SEI with a high content of inorganic components and excellent Li anode performance. We also unveiled the critical role of these electrolytes in maintaining aggregate clusters and enhancing anion decomposition kinetics through the decreased desolvation energy of ions to achieve a homogeneous, high Li_2O content in the SEI enabling the highest CE value of 99.72%. This result brings us a step closer to the ultimate target of 99.9% for the anode-free full cell. This work not only underlines the critical role of Li_2O for high CEs but also the impact of solvation structure controlled through both electrolyte chemistry with judiciously designed diluents and electrolyte engineering to control the composition, morphology, and homogeneity of SEI. These findings are also expected to guide the design of new weakly coordinating diluents to further advance the development of Li metal batteries with high operation voltages.

EXPERIMENTAL PROCEDURES

Resource availability

Lead contact

Further information and requests for resources should be directed to and will be fulfilled by the lead contact, Ali Coskun (ali.coskun@unifr.ch).

Materials availability

All materials generated in this study are available from the [lead contact](#) without restriction.

Data and code availability

All data needed to support the conclusions of this manuscript are included in the main text or the [supplemental information](#). The original data of this study are openly available in Zenodo at <https://doi.org/10.5281/zenodo.7330672>.

SUPPLEMENTAL INFORMATION

Supplemental information can be found online at <https://doi.org/10.1016/j.chempr.2022.12.005>.

ACKNOWLEDGMENTS

A.C. acknowledges the support from the Swiss National Science Foundation (SNF) for funding of this research (200021-188572). J.W.C. acknowledges the support by the National Research Foundation of Korea (NRF) grants (NRF-2021R1A2B5B03001956 and NRF-2018M1A2A2063340), the Technology Innovation Program (20012341) funded by the Ministry of Trade, Industry & Energy (MOTIE) of Korea and generous support from the Institute of Engineering Research (IOER), and Research Institute of Advanced Materials (RIAM) at Seoul National University. L.P.H.J. acknowledges the financial support from the Swiss National Science Foundation (R'Equip program, grant Nr_182987). We would like to thank Dr. Claudia Cancellieri at Empa for XPS support. The authors acknowledge support of the Scientific Center for Optical and Electron Microscopy (ScopeM) of the ETH Zurich. We also thank Dr. Alla Sologubenko and Dr. Stephan Handschin for the cryo-EM test. We also thank Dr. Krzysztof Piech for the DOSY-NMR test.

AUTHOR CONTRIBUTIONS

Y.Z., T.Z., and A.C. designed the concept. Y.Z. synthesized and characterized the molecules. Y.Z. and T.Z. characterized electrolytes and tested electrochemical performance. L.P.H.J. conducted XPS characterizations. X.K. conducted molecular dynamics simulation. Y.Z., T.Z., J.W.C., and A.C. wrote the paper. A.C. and J.W.C. supervised the research. All authors discussed the results and commented on the paper writing.

DECLARATION OF INTERESTS

University of Fribourg, Switzerland and Seoul National University, Republic of Korea filed a patent application for the solvents and electrolytes described in this manuscript. A.C. is a member of the advisory board of *CHEM*.

Received: August 17, 2022

Revised: September 21, 2022

Accepted: December 6, 2022

Published: January 2, 2023

REFERENCES

1. Liu, J., Bao, Z., Cui, Y., Dufek, E.J., Goodenough, J.B., Khalifah, P., Li, Q., Liaw, B.Y., Liu, P., Manthiram, A., et al. (2019). Pathways for practical high-energy long-cycling lithium metal batteries. *Nat. Energy* 4, 180–186. <https://doi.org/10.1038/s41560-019-0338-x>.
2. Choi, J.W., and Aurbach, D. (2016). Promise and reality of post-lithium-ion batteries with high energy densities. *Nat. Rev. Mater.* 1, 16013. <https://doi.org/10.1038/natrevmats.2016.13>.
3. Kwon, T.-w., Choi, J.W., and Coskun, A. (2019). Prospect for supramolecular chemistry in high-energy-density rechargeable batteries. *Joule* 3, 662–682. <https://doi.org/10.1016/j.joule.2019.01.006>.
4. Zheng, X., Huang, L., Ye, X., Zhang, J., Min, F., Luo, W., and Huang, Y. (2021). Critical effects of electrolyte recipes for Li and Na metal batteries. *Chem* 7, 2312–2346. <https://doi.org/10.1016/j.chempr.2021.02.025>.
5. Lin, D., Liu, Y., and Cui, Y. (2017). Reviving the lithium metal anode for high-energy batteries. *Nat. Nanotechnol.* 12, 194–206. <https://doi.org/10.1038/nnano.2017.16>.
6. Fang, C., Wang, X., and Meng, Y.S. (2019). Key issues hindering a practical lithium-metal anode. *J. Trends Chem.* 1, 152–158. <https://doi.org/10.1016/j.trechm.2019.02.015>.

7. Bruce, P.G., Freunberger, S.A., Hardwick, L.J., and Tarascon, J.-M. (2011). Li-O₂ and Li-S batteries with high energy storage. *Nat. Mater.* 11, 19–29. <https://doi.org/10.1038/nmat3191>.
8. Cheng, X.B., Zhang, R., Zhao, C.Z., and Zhang, Q. (2017). Toward safe lithium metal anode in rechargeable batteries: a review. *Chem. Rev.* 117, 10403–10473. <https://doi.org/10.1021/acs.chemrev.7b00115>.
9. Zhang, X., Yang, Y., and Zhou, Z. (2020). Towards practical lithium-metal anodes. *Chem. Soc. Rev.* 49, 3040–3071. <https://doi.org/10.1039/c9cs00838a>.
10. Liu, B., Zhang, J.-G., and Xu, W. (2018). Advancing lithium metal batteries. *Joule* 2, 833–845. <https://doi.org/10.1016/j.joule.2018.03.008>.
11. Zhang, J.G., Xu, W., Xiao, J., Cao, X., and Liu, J. (2020). Lithium metal anodes with nonaqueous electrolytes. *Chem. Rev.* 120, 13312–13348. <https://doi.org/10.1021/acs.chemrev.0c00275>.
12. Liu, S., Ji, X., Piao, N., Chen, J., Eidson, N., Xu, J., Wang, P., Chen, L., Zhang, J., Deng, T., et al. (2021). An inorganic-rich solid electrolyte interphase for advanced lithium-metal batteries in carbonate electrolytes. *Angew. Chem. Int. Ed. Engl.* 60, 3661–3671. <https://doi.org/10.1002/anie.202012005>.
13. Schweidler, S., de Biasi, L., Schiele, A., Hartmann, P., Brezesinski, T., and Janek, J. (2018). Volume changes of graphite anodes revisited: a combined operando X-ray diffraction and in situ pressure analysis study. *J. Phys. Chem. C* 122, 8829–8835.
14. Qian, J., Henderson, W.A., Xu, W., Bhattacharya, P., Engelhard, M., Borodin, O., and Zhang, J.G. (2015). High rate and stable cycling of lithium metal anode. *Nat. Commun.* 6, 6362. <https://doi.org/10.1038/ncomms7362>.
15. Aurbach, D., Zaban, A., Schechter, A., Ein-Eli, Y., Zinigrad, E., and Markovsky, B. (1995). The study of electrolyte solutions based on ethylene and diethyl carbonates for rechargeable Li batteries: I. Li metal anodes. *J. Electrochem. Soc.* 142, 2873–2882.
16. Zhou, T., Zhao, Y., El Kazzi, M., Choi, J.W., and Coskun, A. (2021). Stable solid electrolyte interphase formation induced by monoquat-based anchoring in lithium metal batteries. *ACS Energy Lett.* 6, 1711–1718. <https://doi.org/10.1021/acsenergylett.1c00274>.
17. Zhang, X.Q., Chen, X., Cheng, X.B., Li, B.Q., Shen, X., Yan, C., Huang, J.Q., and Zhang, Q. (2018). Highly stable lithium metal batteries enabled by regulating the solvation of lithium ions in nonaqueous electrolytes. *Angew. Chem. Int. Ed. Engl.* 130, 5399–5403.
18. Ren, X., Zhang, Y., Engelhard, M.H., Li, Q., Zhang, J.-G., and Xu, W. (2018). Guided lithium metal deposition and improved lithium coulombic efficiency through synergistic effects of LiAsF₆ and cyclic carbonate additives. *ACS Energy Lett.* 3, 14–19.
19. Wang, Q., Yao, Z., Zhao, C., Verhallen, T., Tabor, D.P., Liu, M., Ooms, F., Kang, F., Aspuru-Guzik, A., and Hu, Y.-S. (2020). Interface chemistry of an amide electrolyte for highly reversible lithium metal batteries. *Nat. Commun.* 11, 4188.
20. Fang, C., Li, J., Zhang, M., Zhang, Y., Yang, F., Lee, J.Z., Lee, M.H., Alvarado, J., Schroeder, M.A., Yang, Y., et al. (2019). Quantifying inactive lithium in lithium metal batteries. *Nature* 572, 511–515. <https://doi.org/10.1038/s41586-019-1481-z>.
21. Aurbach, D., and Granot, E. (1997). The study of electrolyte solutions based on solvents from the “glyme” family (linear polyethers) for secondary Li battery systems. *Electrochim. Acta* 42, 697–718.
22. Aurbach, D., Pollak, E., Elazari, R., Salitra, G., Kelley, C.S., and Affinito, J. (2009). On the surface chemical aspects of very high energy density, rechargeable Li-sulfur batteries. *J. Electrochem. Soc.* 156, A694. <https://doi.org/10.1149/1.3148721>.
23. Jaumann, T., Balach, J., Klose, M., Oswald, S., Eckert, J., and Giebeler, L. (2016). Role of 1,3-dioxolane and LiNO₃ addition on the long term stability of nanostructured silicon/carbon anodes for rechargeable lithium batteries. *J. Electrochem. Soc.* 163, A557–A564.
24. Wang, J., Huang, W., Pei, A., Li, Y., Shi, F., Yu, X., and Cui, Y. (2019). Improving cyclability of Li metal batteries at elevated temperatures and its origin revealed by cryo-electron microscopy. *Nat. Energy* 4, 664–670. <https://doi.org/10.1038/s41560-019-0413-3>.
25. Amanchukwu, C.V., Yu, Z., Kong, X., Qin, J., Cui, Y., and Bao, Z. (2020). A new class of ionically conducting fluorinated ether electrolytes with high electrochemical stability. *J. Am. Chem. Soc.* 142, 7393–7403. <https://doi.org/10.1021/jacs.9b11056>.
26. Yu, Z., Wang, H., Kong, X., Huang, W., Tsao, Y., Mackanic, D.G., Wang, K., Wang, X., Huang, W., Choudhury, S., et al. (2020). Molecular design for electrolyte solvents enabling energy-dense and long-cycling lithium metal batteries. *Nat. Energy* 5, 526–533. <https://doi.org/10.1038/s41560-020-0634-5>.
27. Yao, Y.X., Chen, X., Yan, C., Zhang, X.Q., Cai, W.L., Huang, J.Q., and Zhang, Q. (2021). Regulating interfacial chemistry in lithium-ion batteries by a weakly solvating electrolyte. *Angew. Chem. Int. Ed. Engl.* 60, 4090–4097.
28. Wang, H., Yu, Z., Kong, X., Huang, W., Zhang, Z., Mackanic, D.G., Huang, X., Qin, J., Bao, Z., and Cui, Y. (2021). Dual-solvent Li-ion solvation enables high-performance Li-metal batteries. *Adv. Mater.* 33. <https://doi.org/10.1002/adma.202008619>.
29. Jiao, S., Ren, X., Cao, R., Engelhard, M.H., Liu, Y., Hu, D., Mei, D., Zheng, J., Zhao, W., Li, Q., et al. (2018). Stable cycling of high-voltage lithium metal batteries in ether electrolytes. *Nat. Energy* 3, 739–746. <https://doi.org/10.1038/s41560-018-0199-8>.
30. Ren, X., Zou, L., Cao, X., Engelhard, M.H., Liu, W., Burton, S.D., Lee, H., Niu, C., Matthews, B.E., Zhu, Z., et al. (2019). Enabling high-voltage lithium-metal batteries under practical conditions. *Joule* 3, 1662–1676. <https://doi.org/10.1016/j.joule.2019.05.006>.
31. Wang, J., Yamada, Y., Sodeyama, K., Chiang, C.H., Tateyama, Y., and Yamada, A. (2016). Superconcentrated electrolytes for a high-voltage lithium-ion battery. *Nat. Commun.* 7, 12032. <https://doi.org/10.1038/ncomms12032>.
32. Cao, X., Ren, X., Zou, L., Engelhard, M.H., Huang, W., Wang, H., Matthews, B.E., Lee, H., Niu, C., Arey, B.W., et al. (2019). Monolithic solid-electrolyte interphases formed in fluorinated orthoformate-based electrolytes minimize Li depletion and pulverization. *Nat. Energy* 4, 796–805. <https://doi.org/10.1038/s41560-019-0464-5>.
33. Ren, X., Chen, S., Lee, H., Mei, D., Engelhard, M.H., Burton, S.D., Zhao, W., Zheng, J., Li, Q., Ding, M.S., et al. (2018). Localized high-concentration sulfone electrolytes for high-efficiency lithium-metal batteries. *Chem* 4, 1877–1892. <https://doi.org/10.1016/j.chempr.2018.05.002>.
34. Cao, X., Gao, P., Ren, X., Zou, L., Engelhard, M.H., Matthews, B.E., Hu, J., Niu, C., Liu, D., Arey, B.W., et al. (2021). Effects of fluorinated solvents on electrolyte solvation structures and electrode/electrolyte interphases for lithium metal batteries. *Proc. Natl. Acad. Sci. USA* 118. <https://doi.org/10.1073/pnas.2020357118>.
35. Ren, X., Gao, P., Zou, L., Jiao, S., Cao, X., Zhang, X., Jia, H., Engelhard, M.H., Matthews, B.E., Wu, H., et al. (2020). Role of inner solvation sheath within salt-solvent complexes in tailoring electrode/electrolyte interphases for lithium metal batteries. *Proc. Natl. Acad. Sci. USA* 117, 28603–28613. <https://doi.org/10.1073/pnas.2010852117>.
36. Li, Y., Li, Y., Pei, A., Yan, K., Sun, Y., Wu, C.L., Joubert, L.M., Chin, R., Koh, A.L., Yu, Y., et al. (2017). Atomic structure of sensitive battery materials and interfaces revealed by cryo-electron microscopy. *Science* 358, 506–510. <https://doi.org/10.1126/science.aam6014>.
37. Li, Y., Huang, W., Li, Y., Pei, A., Boyle, D.T., and Cui, Y. (2018). Correlating structure and function of battery interphases at atomic resolution using cryoelectron microscopy. *Joule* 2, 2167–2177. <https://doi.org/10.1016/j.joule.2018.08.004>.
38. Huang, W., Wang, H., Boyle, D.T., Li, Y., and Cui, Y. (2020). Resolving nanoscopic and mesoscopic heterogeneity of fluorinated species in battery solid-electrolyte interphases by cryogenic electron microscopy. *ACS Energy Lett.* 5, 1128–1135. <https://doi.org/10.1021/acsenergylett.0c00194>.
39. Guo, R., and Gallant, B.M. (2020). Li₂O solid electrolyte interphase: probing transport properties at the chemical potential of lithium. *Chem. Mater.* 32, 5525–5533. <https://doi.org/10.1021/acs.chemmater.0c00333>.
40. Adams, B.D., Zheng, J., Ren, X., Xu, W., and Zhang, J.G. (2018). Accurate determination of Coulombic efficiency for lithium metal anodes and lithium metal batteries. *Adv. Energy Mater.* 8, 1702097.
41. Ren, X., Zou, L., Jiao, S., Mei, D., Engelhard, M.H., Li, Q., Lee, H., Niu, C., Adams, B.D., Wang, C., et al. (2019). High-concentration ether electrolytes for stable high-voltage lithium metal batteries. *ACS Energy Lett.* 4, 896–902.
42. Fan, X., Chen, L., Borodin, O., Ji, X., Chen, J., Hou, S., Deng, T., Zheng, J., Yang, C., Liou, S.C., et al. (2018). Non-flammable electrolyte enables Li-metal batteries with aggressive

- cathode chemistries. *Nat. Nanotechnol.* **13**, 715–722.
43. Chen, S., Zheng, J., Mei, D., Han, K.S., Engelhard, M.H., Zhao, W., Xu, W., Liu, J., and Zhang, J.G. (2018). High-voltage lithium-metal batteries enabled by localized high-concentration electrolytes. *Adv. Mater.* **30**, e1706102.
44. Ganguly, B., and Fuchs, B. (2001). Probing the influence of stereoelectronic effects on lithium affinity in 1,3- and 1,4-dioxane systems. *J. Phys. Org. Chem.* **14**, 488–494. <https://doi.org/10.1002/poc.397>.
45. Zhu, Y., Pande, V., Li, L., Wen, B., Pan, M.S., Wang, D., Ma, Z.-F., Viswanathan, V., and Chiang, Y.-M. (2020). Design principles for self-forming interfaces enabling stable lithium-metal anodes. *Proc. Natl. Acad. Sci. USA* **117**, 27195–27203.
46. Wang, M., Huai, L., Hu, G., Yang, S., Ren, F., Wang, S., Zhang, Z., Chen, Z., Peng, Z., and Shen, C. (2018). Effect of LiFSI concentrations to form thickness-and modulus-controlled SEI layers on lithium metal anodes. *J. Phys. Chem. C* **122**, 9825–9834.
47. Wu, B., Lochala, J., Taverne, T., and Xiao, J. (2017). The interplay between solid electrolyte interface (SEI) and dendritic lithium growth. *Nano Energy* **40**, 34–41.
48. Zeng, X., Xu, G.-L., Li, Y., Luo, X., Maglia, F., Bauer, C., Lux, S.F., Paschos, O., Kim, S.-J., Lamp, P., et al. (2016). Kinetic study of parasitic reactions in lithium-ion batteries: a case study on $\text{LiNi}_{0.6}\text{Mn}_{0.2}\text{Co}_{0.2}\text{O}_2$. *ACS Appl. Mater. Interfaces* **8**, 3446–3451.
49. Vadivel, N.R., Ha, S., He, M., Dees, D., Trask, S., Polzin, B., and Gallagher, K.G. (2017). On leakage current measured at high cell voltages in lithium-ion batteries. *J. Electrochem. Soc.* **164**, A508–A517.
50. Yamada, Y., Yaegashi, M., Abe, T., and Yamada, A. (2013). A superconcentrated ether electrolyte for fast-charging Li-ion batteries. *Chem. Commun. (Camb)* **49**, 11194–11196.
51. Jiang, Z., Zeng, Z., Liang, X., Yang, L., Hu, W., Zhang, C., Han, Z., Feng, J., and Xie, J. (2021). Fluorobenzene, a low-density, economical, and bifunctional hydrocarbon cosolvent for practical lithium metal batteries. *Adv. Funct. Mater.* **31**, 2005991.
52. Yu, Z., Rudnicki, P.E., Zhang, Z., Huang, Z., Celik, H., Oyakhire, S.T., Chen, Y., Kong, X., Kim, S.C., Xiao, X., et al. (2022). Rational solvent molecule tuning for high-performance lithium metal battery electrolytes. *Nat. Energy* **7**, 94–106. <https://doi.org/10.1038/s41560-021-00962-y>.